Supporting Information

Samanta et al. 10.1073/pnas.1219666110

SI Text

Sample Preparation and Characterization

The fluid was prepared by adding the required quantity of polymers to 30 L of distilled water. The solution was gently stirred for 48 h, and measurements were performed within a week. The solutions were characterized by means of a commercial rheometer (MARS II; Thermo Fisher Scientific) in controlled shear rate mode using a cone and plate geometry (diameter = 60 mm, cone angle = 0.5°). The instrument was set to a temperature of $T = 20$ °C, which is the same temperature the pipe flow experiments were conducted at. The solutions were tested before and after the measurements in the pipe; in addition, we tested samples that were prepared in smaller quantities (250 mL) by means of the same protocol mentioned above. The results for the different solutions agreed within an experimental resolution of $\pm 5\%$ and in agreement with former studies (1). Specifically, we did not observe any notable degradation of the polymer on the time scale of resident times in the tube experiments, in the rheological shear tests, or in the capillary breakup extensional rheometer (CaBER). The viscosity was measured at shear rates $30 \text{ s} < \dot{\gamma} < 2,500 \text{ s}^{-1}$ for polymer concentrations of 50 ppm, 100 ppm, 200 ppm, 300 ppm, 400 ppm, and 500 ppm. The effect of shear thinning is negligible [i.e., the respective power law coefficients were very small (<0.026, compare Fig. S1)]. The (zero-)shear viscosity η increases with the polymer concentration c and from the dilution series, we can extract an overlap concentration of $c^* \approx 1,280$ ppm (compare Fig. S2) via a quadratic fit satisfying $[\eta] = \lim_{c \to 0} (\eta(c) - \eta_s)/\eta_s = 1/c^*$ (2).

In addition, the pressure drop in the pipe in the laminar case was calculated by means of the measured viscosity data and with the assumption of a parabolic flow profile. Again, the calculated values and the measured pressure drops agreed within $\pm 5\%$. The Reynolds number (Re) was determined by means of the viscosity of the sample solution (i.e., $Re = \rho U D / \eta$).

The second rheological characterization was performed with a custom-built CaBER (3) at ambient temperature ($T \approx 23$ °C). A droplet of the sample was placed between two steel plates, from which the upper one is displaced by a linear motor until the capillary bridge becomes unstable due to the Rayleigh–Plateau instability. In the following thinning process, a parallel filament is formed that shrinks exponentially in time. The characteristic time scale of the thinning process λ_C (compare Fig. S3) can be related to the polymer relaxation time λ. Simple models predict $\lambda = 3\lambda_C$, but it has been shown that the relation is much more complex in reality (1, 4). However, the CaBER is still most sensitive to the elasticity of diluted aqueous solutions, and the time scale λ_C is commonly used to define a Weissenberg number (Wi) (5). The relaxation time λ_C depends on the concentration c according to a power law $\lambda_C \propto c^{0.89 \pm 0.03}$ (1). The nonlinear fit was performed by direct weighting of the data to account for the increasing sparseness of filament data when decreasing the polymer concentrations and relaxation time, respectively. The error bars represent the SE of the measurement series of each concentration.

From the CaBER relaxation times, an estimate of the critical Weissenberg numbers (Wi_c) can be made, and we found that the Wi_c were in the range of $Wi_c = 3 - 15$.

Velocity Measurements

Velocity measurements were carried out with particle image velocimetry in the $D = 4$-mm pipe. The flow was illuminated in the mid r-z plane (with z being the axial direction and r being the radial direction) using a laser light sheet for the experiments with polymer solution and a high-power light-emitting diode for the experiments with water, respectively. The fluid was seeded with 13-μm spherical hollow glass spheres to obtain particle images. Sampling rates of the camera (Phantom V10; Vision Research) were 200 Hz for the polymer experiments and 50 Hz for the case of water. In Fig. S4, we show the z component of the velocity measured at the pipe centerline: In the case of water, the theoretical value of the centerline velocity for a laminar velocity profile for the given Reynolds number has been subtracted, and in the case of polymer, the average velocity has been subtracted. At $Re = 527$, the flow in the 500-ppm polyacrylamide solution is laminar. Once the Re is raised above 800, elasto-inertial turbulence (EIT) sets in and fluctuations start to increase with the Re (Fig. S4B). As shown in Fig. 4B for $Re = 2,140$, the flow is uniformly fluctuating. For a water flow with a similar $Re = 2,080$ (Fig. S4C), however, flows show the intermittency distinctive of the transitional regime in Newtonian turbulence, with turbulent puffs (characterized by a strong dip of the centerline velocity) interspersed by more quiescent flow.

Initial Perturbations for Direct Numerical Simulations

The protocol for our simulation was designed to mimic the perturbed experimental setup within the limitation inherent to boundary conditions. For any flow, Newtonian or polymeric, the laminar solution is first obtained. Once the laminar flow is fully developed, a perturbation is introduced over a short duration, in the form of blowing and suction velocity on both walls, over which white noise of prescribed intensity is introduced. The velocity pattern is periodic in x and z:

$$v_w(x, z, t) = A \sin\left(\frac{8\pi}{L_x} x\right) \sin\left(\frac{8\pi}{L_z} z\right) + \varepsilon(t), \qquad \textbf{[S1]}$$

where A is the amplitude, Lx and L_z are the horizontal domain dimensions, and $\varepsilon(t)$ is the random noise. The amplitude is increased from zero over the first 10% of the duration of the perturbation and decreased to zero over the last 10%. Choosing $A = 0.09 U_b$ and the rms of ε at $0.005 U_b$ causes the Newtonian flow to transition at $Re = 6,000$. The total duration of the perturbation is $0.5 H/U_b$.

Polymer Extension

Fig. S5 shows profiles of polymer extension, defined as

$$\frac{X}{L} = \frac{\sqrt{\text{tr}(\mathbf{C})}}{L}, \qquad \textbf{[S2]}$$

across the channel half-height. The extension of polymers at the lowest Re is just shy of 20% of maximum polymer extension. At 17.4%, the wall polymer extension is higher than the analytical solution for a purely laminar channel flow (16.2%), due to the fluctuations of the velocity gradient tensor caused by EIT. Single-molecule experiments measured extension in shear flow, at $Wi = 25$, around 30% (6, 7). This discrepancy comes from the semiquantitative nature of the finitely extensible nonlinear elastic Peterlin (FENE-P) model. The choice of the polymer parameters is a compromise between capturing the key dynamical features of polymer–flow interactions and numerical stability. Among others, Li et al. (8), Housiadas and Beris (9), and Tamano et al. (10) studied the effects of rheological parameters and viscoelastic models. The conclusions of these studies are that (a)

elongational viscosity is the most important rheological property and (b) long polymers and a large Wi are more likely to reproduce the features of polymer drag reduction, especially maximum drag reduction. It is noteworthy that simulations with a smaller polymer $L = 100$, which yields a wall extension of 30%, were also found to produce EIT. Our choice of polymer length was motivated by the fact that using longer polymers emphasizes the elastic instability and facilitates the study of EIT while retaining the same dynamics as with $L = 100$.

Identification of the Structure of Elasto-inertial Instability

Fig. 4 shows an interesting pattern of flow instabilities in the form of quasi-2D patterns aligned in the streamwise direction. The identification of the flow structures is made possible by the visualization of isosurfaces of Q, the second invariant of the velocity gradient tensor $\nabla\mathbf{u}$. Defining the velocity gradient tensor as $\nabla\mathbf{u} = \partial u_i / \partial x_j$, the second and third R invariants are written as

$$Q = -\frac{1}{2}\frac{\partial u_i}{\partial x_j}\frac{\partial u_j}{\partial x_i} \ , \qquad \text{[S3]}$$

$$R = -\frac{1}{3}\frac{\partial u_i}{\partial x_j}\frac{\partial u_j}{\partial x_k}\frac{\partial u_k}{\partial x_i} \ , \qquad \text{[S4]}$$

where Einstein's index rule applies. Q and R are used to study the topology of turbulent flows (11) because their local values relate to the local topology of the streamlines. This is illustrated in Fig. S6 in the $Q - R$ phase diagram that defines four quadrants delimited by $R = 0$ and $D = 0$, where D is the discriminant of $\nabla\mathbf{u}$:

$$D = \frac{27}{4}R^2 + Q^3 \ . \qquad \text{[S5]}$$

It can also be shown that Q is the difference between the norm squared of the rotation and strain rate tensors, which suggests that positive regions of Q are regions where the local rotation rate overcomes the strain rate. This argument is the motivation for the widespread use of the positive Q criterion (12) for the identification of vortices. However, it is important to point out that the Q-vortex identification method is subjective, because the proper reduction of vortices requires that $Q > Q_{\text{th}}$, where Q_{th} is a positive threshold that depends on the flow intensity.

The local topology of the flow determines the stretching dynamics of the polymer field. Specifically, extensional flows cause the polymer to stretch, thereby increasing the local extensional viscosity, which is, for instance, the source of polymer drag reduction (13). At $Re = 1{,}000$ (Fig. 4 and Fig. S7A), compact regions of positive Q do not define vortices because they fail to meet the criterion of spiraling streamlines (12). Nonetheless, the contours of D (Fig. S7A) clearly show that the isosurfaces of positive and negative Q are regions of weakly rotational and extensional flows in regions of large polymer extension, as shown by Fig. S7B. These fluctuations of extensional flow create, in turn, fluctuations of extensional viscosity that directly affect the flow. Note that the computational grid is displayed in Fig. 7A to demonstrate that the elastic instability is well resolved. In this particular case, the grid spacing in x is $\approx 1 l^+ = \nu/u_\tau$.

1. Zell A, Gier S, Rafai S, Wagner C (2010) Is there a relation between the relaxation time measured in CaBER experiments and the first normal stress coefficient? *J Nonnewton Fluid Mech* 165:1265–1274.
2. Kozicki W, Kuang PQ (1996) An alternative method for evaluation of intrinsic viscosity. *Can J Chem Eng* 74:429–432.
3. Anna SL, McKinley GH (2001) Elasto-capillary thinning and breakup of model elastic liquids. *J Rheol (N Y N Y)* 45:115–138.
4. Clasen C, et al. (2006) How dilute are dilute solutions in extensional flows? *J Rheol (N Y N Y)* 50:849.
5. Rodd LE, Scott TP, Boger DV, Cooper-White JJ, McKinley GH (2005) The inertio-elastic planar entry flow of low-viscosity elastic fluids in micro-fabricated geometries. *J Nonnewton Fluid Mech* 129:1–22.
6. Smith DE, Babcock HP, Chu S (1999) Single-polymer dynamics in steady shear flow. *Science* 283:5408.
7. Gerashchenko S, Steinberg V (2006) Statistics of tumbling of a single polymer molecule in shear flow. *Phys Rev Lett* 96(3):038304.
8. Li C-F, Sureshkumar R, Khomami B (2006) Influence of rheological parameters on polymer induced turbulent drag reduction. *J Nonnewton Fluid Mech* 140:2340.
9. Housiadas KD, Beris AN (2006) Extensional behavior influence on viscoelastic turbulent channel flow. *J Nonnewton Fluid Mech* 140(1-3):4156.
10. Tamano S, Itoh M, Hotta S, Yokota K, Morinishi Y (2009) Effect of rheological properties on drag reduction in turbulent boundary layer flow. *Phys Fluids* 21:055101.
11. Chong MS, et al. (1998) Turbulence structures of wall-bounded shear flows found using DNS data. *J Fluid Mech* 357:225–247.
12. Dubief Y, Delcayre F (2000) On coherent-vortex identification in turbulence. *Journal of Turbulence* 1(1):11.
13. Terrapon VE, Dubief Y, Moin P, Shaqfeh ESG, Lele SK (2004) Simulated polymer stretch in a turbulent flow using Brownian dynamics. *J Fluid Mech* 504:61–71.
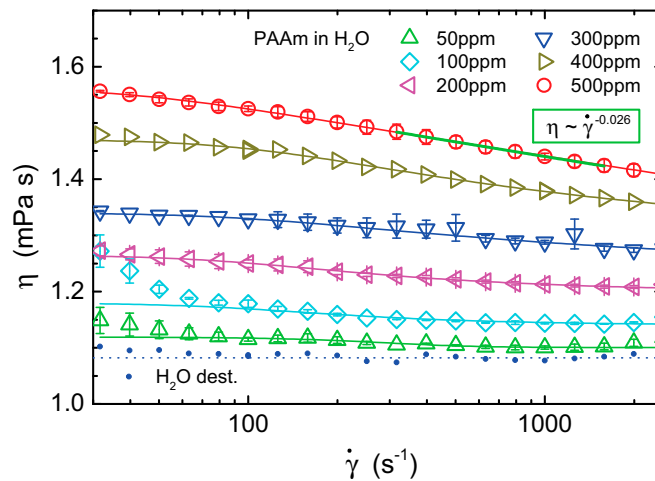
Fig. S1. Shear viscosities of the polymer solutions measured at shear rates between 30 s^{-1} and 2,500 s^{-1} for solutions of 50 ppm, 100 ppm, 200 ppm, 300 ppm, 400 ppm, and 500 ppm at T = 20 °C. Shear thinning is of little importance. Also shown is a reference measurement with pure water.
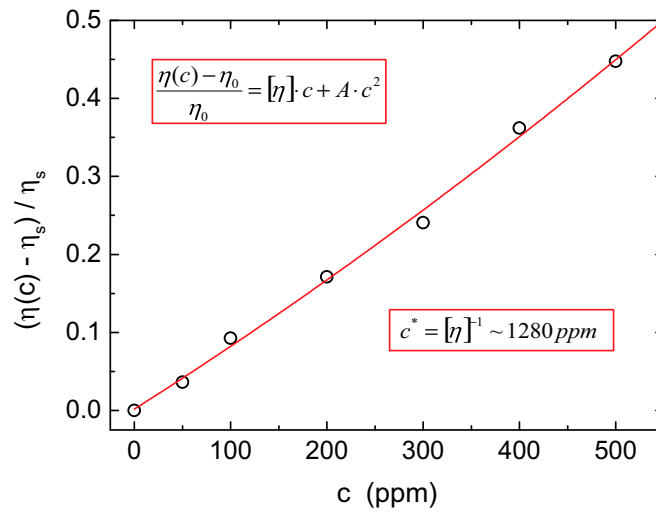
Fig. S2. Specific (zero)-shear viscosity of the polymer solutions for different concentrations. The overlap concentration is estimated to be $c^* \approx 1,280$ ppm.

$$\frac{\eta(c) - \eta_0}{\eta_0} = [\eta] \cdot c + A \cdot c^2$$
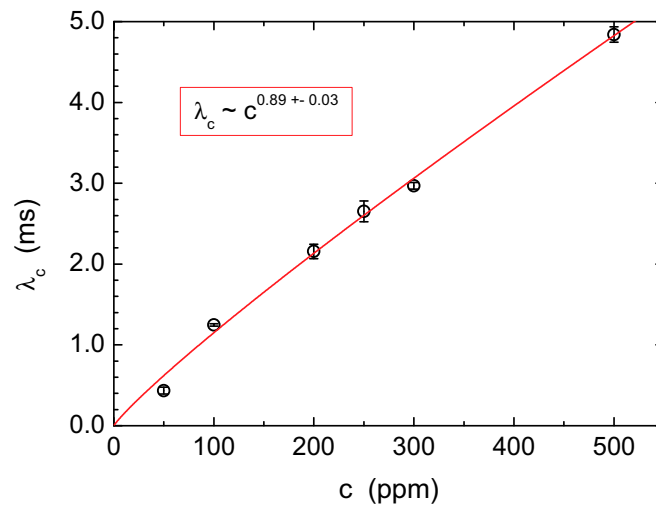
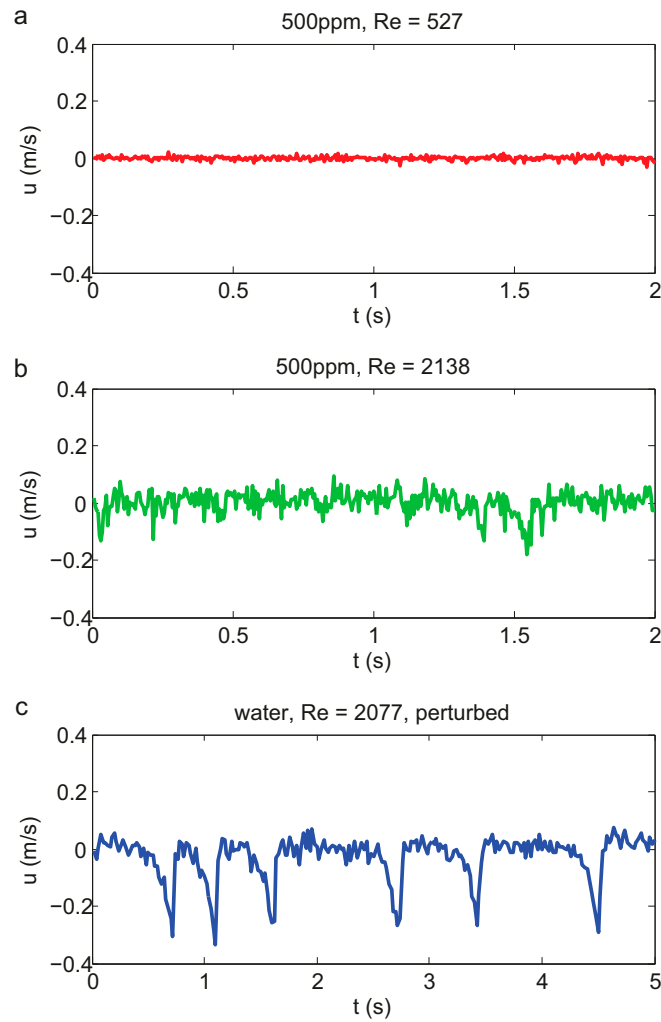$$c^* = [\eta]^{-1} \sim 1280\, ppm$$

Fig. S3. Characteristic relaxation time λ_C of the polymer solutions in the CaBER experiments. It scales with the polymer concentration c with a power law with an exponent of 0.89 ± 0.03.

$$\lambda_c \sim c^{0.89 +- 0.03}$$

Fig. S4. Velocity time series. (*A*) Centerline velocity of laminar flow in a 500-ppm polymer solution at *Re* = 530. (*B*) Velocity time series in the elasto-inertial turbulent regime at *Re* = 2,140. (*C*) Velocity trace in a pure water flow at *Re* = 2,080 shows the intermittent appearance of turbulent puffs typical of Newtonian turbulence.
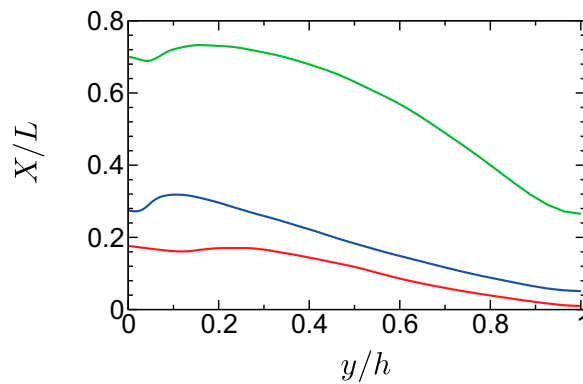
Fig. S5. Profiles of polymer extension defined by $X/L = \sqrt{\text{tr}(\mathbf{C})/L^2}$ as a function of the distance from the wall normalized by the half-height of the channel y/h. Red line, *Re* = 1,000, *Wi* = 24; blue line, *Re* = 6,000, *Wi* = 100; green line, *Re* = 6,000, *Wi* = 700.
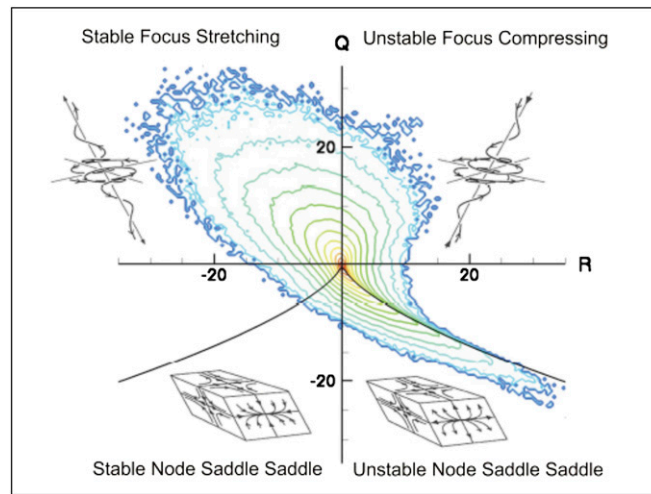
Fig. S6. Flow topology in the $Q - R$ phase diagram [Reprinted with permission from the study by Chong et al. (13)], with the typical inverted teardrop shape of a joint-probability density function of a turbulent flow. The figure shows the four quadrants of flow topology delimited by $R = 0$ and $D = 0$ (Eq. **S5**), from $(R > 0, D > 0)$ counterclockwise: rotational flow under compression, rotational flow under extension, biaxial compressional flow, and biaxial extensional flow.
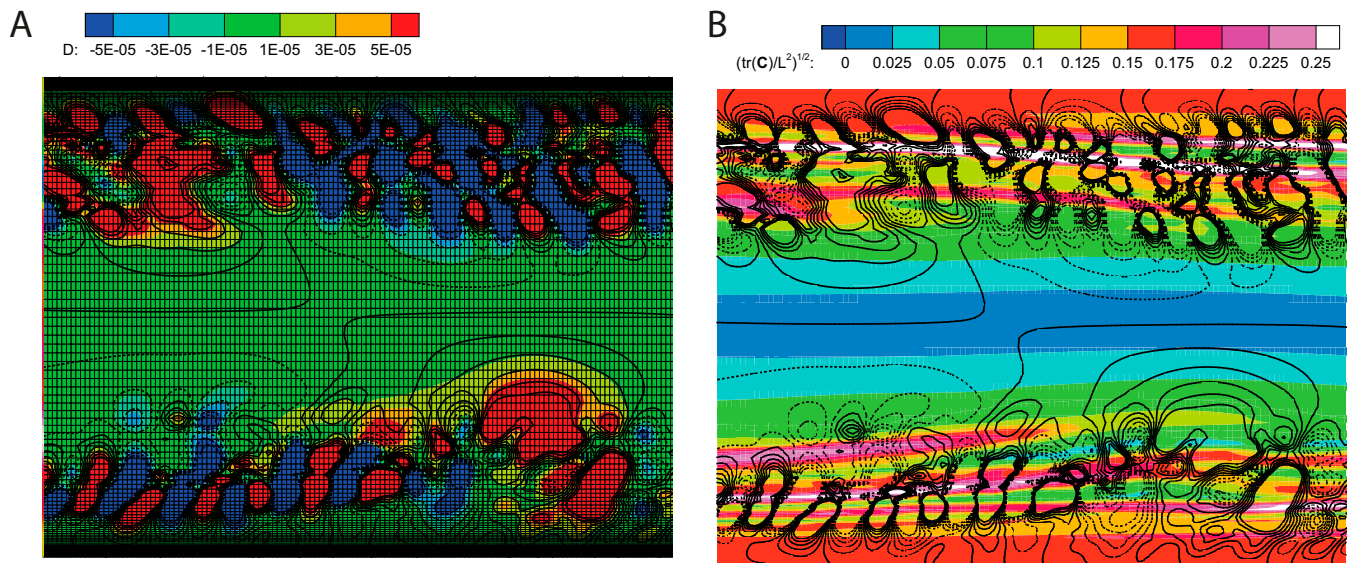
Fig. S7. Visualization of the instability observed in Fig. 4 in a cross-sectional plane of the flow (left to right) for about one-fourth of the length of the domain. The walls are the top and lower boundaries. (*A*) Contours of positive (solid black lines) and negative (dashed black lines) Q superimposed over the contours of positive (red) and negative (blue) D in a cross-sectional plane of the flow aligned with the streamwise and wall-normal directions. The grid is shown to demonstrate that the observed instability is fully resolved. (*B*) Contour lines are the same as in *A*, with contours of the polymer extension.